Talanta 165 (2017) 297–303

Contents lists available at ScienceDirect

Talanta

journal homepage: www.elsevier.com/locate/talanta

A supramolecular material for dual-modal imaging and targeted cancer therapy

Shanyue Guan[a,b], Ruizheng Liang[a], Chunyang Li[a], Min Wei[a,*]

[a] State Key Laboratory of Chemical Resource Engineering, Beijing University of Chemical Technology, Beijing 100029, PR China
[b] Key Laboratory of Photochemical Conversion and Optoelectronic Materials, Technical Institute of Physics and Chemistry, Chinese Academy of Sciences, Beijing 100190, PR China

ARTICLE INFO

Keywords:
Supramolecular
Dual-modal imaging
Chemotherapy

ABSTRACT

Recently, how to design a formulation system with simultaneous diagnosis and therapy toward cancer has attracted tremendous attention. Herein, a supramolecular material was prepared *via* a facile method by the co-intercalation of folic acid (FA) and doxorubicin (DOX) into the gallery of Gd^{3+}-doped layered double hydroxides (LDHs), followed by surface adsorption of fluorescein isothiocyanate (FITC). This supramolecular agent was proved to exhibit excellent magnetic resonance imaging (MRI) and fluorescence imaging (FI) behavior, as well as chemotherapy toward cancer (KB cell). The co-intercalated FA enables an efficient and selective drug delivery with good specificity. This work provides a facile approach for the fabrication of a drug formulation with dual-modal imaging and targeted therapy, which could be potentially used in the practical chemotherapy and medical imaging.

1. Introduction

A theranostic platform for simultaneous diagnosis and therapy has been explored over the decades [1,2]. The common diagnosis methods include magnetic resonance imaging (MRI) [3,4], computed tomography (CT) [5,6], positron emission tomography (PET) [7,8], photoacoustic imaging (PAT) [9,10] and fluorescence imaging [11]. However, owing to the limit of each individual imaging modality, a single methodology is rarely sufficient to provide high resolution and sensitivity [12]. For instance, fluorescence imaging is an essential technique for the biomedical investigations owing to its excellent sensitivity, but it lacks spatial and anatomical resolution. MRI presents high spatial resolution, but suffers from limited sensitivity [13,14]. Thus, the integration of multimodal imaging strategies for the purpose of achieving a synergistic imaging modality has attracted considerable research interest [15].

Chemotherapy is one of the most widely applied cancer treatments [16], but traditional chemotherapeutic agents lack of specificity to target at diseased regions and thus lead to undesired side effects to normal tissues [17,18]. Therefore, modeling chemotherapeutic drugs by virtue of a biocompatible and targeted drug delivery vehicle is highly necessary, so as to decrease side effects and enhance the tumor accumulation [19]. More interestingly, a combination of imaging agents and chemotherapeutic drugs into one platform with simultaneous diagnosis and therapy has drawn tremendous attention [20,21]. A various of nanocarriers such as Fe_3O_4 nanoparticles (NPs) [22,23], Au NPs [24,25], Upconversion NPs [6,26,27], graphene oxide NPs [28], were synthesized for the simultaneous bioimaging and cancer therapy. Nevertheless, these nanocarriers normally suffer from laborious preparation, limited loading capacity, or weak biocompatibility. Therefore, it is a major challenge to explore highly efficient drug formulation systems for simultaneous multimodal imaging and cancer therapy.

Layered double hydroxides (LDHs) are a typical class of layered materials represented by the general formula $[M^{2+}_{1-x}M^{3+}_{x}(OH)_2](A^{n-})_{x/n}\cdot mH_2O$ [29], which contains positively charged brucite-like layers and charge balancing anions between the host layers [30,31]. By virtue of its unique structure, LDHs have been explored as drug delivery and controlled release vehicle with enhanced cellular uptake and good biodegradation [32,33]. Moreover, the biocompatibility of LDHs has been demonstrated, which is almost nontoxic for normal cells as high as 1 mg/mL [34,35]. This motivates us to develop a dual-modal imaging and targeted cancer therapy based on LDHs supramolecular assembly: (1) doping Gd^{3+} in LDHs host layers and stabilizing fluorescein isothiocyanate (FITC) on LDHs surface for MRI and fluorescence dual-modal imaging; (2) co-intercalating chemotherapy drug (doxorubicin, DOX) and targeting agent (folic acid, FA) into the interlayer gallery of LDHs for targeted cancer therapy. This supramo-

* Corresponding author.
E-mail addresses: liangruizheng2000@163.com (R. Liang), weimin@mail.buct.edu.cn (M. Wei).

http://dx.doi.org/10.1016/j.talanta.2016.12.068
Received 26 August 2016; Received in revised form 19 December 2016; Accepted 24 December 2016
Available online 25 December 2016

lecular drug formulation would show the following advantages: (i) the host layer provides dual docking sites for chemically-coordinated Gd^{3+} and electrostatically-adsorbed FITC, which endows good MRI and enhanced fluorescence imaging; (ii) the host-guest interactions could improve the stability and hydrophilicity of DOX, enhancing the drug permeability. In addition, the over-expression of FA toward cancer cells would increase the drug uptake.

In this work, a layered FITC/FA-DOX/Gd-LDHs material was synthesized through co-intercalation of FA and DOX into the interlayer gallery of Gd^{3+}-doped LDH, followed by surface adsorption of FITC, which shows satisfactory dual-modal imaging and anticancer behavior with targeted ability. XRD and UV–vis spectroscopy confirm that DOX and FA molecules are co-intercalated in the interlayer region of Gd-LDHs matrix. FT-IR and photoluminescence (PL) spectra testify the incorporation of FITC. The high-spin Gd^{3+} in LDHs host layers is conducive to trigger the longitudinal relaxivity, resulting in the positive contrast enhancement for T_1-MRI. Both satisfactory dual-modal imaging and anticancer behavior are demonstrated for the FITC/FA-DOX/Gd-LDHs over *in vitro* tests performed with KB cells, with the half maximal inhibitory concentration (IC_{50}) as low as 5.00 μg/mL at 48 h. In addition, this drug displays a high storage stability, good biocompatibility and targeting capability, which would be favorable for its potential practical application.

2. Results and discussion

2.1. Structural and morphological characterization

DOX and FA were co-intercalated into the interlayer region of Gd-LDH *via* separate nucleation and aging steps (SNAS) method developed by our group [36], in which Gd^{3+} as a MRI agent was doped into the host layers of LDH; FITC was further adsorbed by the host layers through electrostatic interaction. Scheme 1 illustrates the structural model of resulting DOX/FITC-FA/Gd-LDH. Since the doping amount of Gd (denoted as Gd(*x*%)-LDH) influences the LDH structure while the loading amount of FITC (denoted as FITC(*y*%)/LDH) determines its aggregation state and fluorescence property, these two parameters were firstly investigated. A series of Gd(*x*%)-LDHs are prepared and their XRD and FT-IR patterns are shown in Fig. S1a and b, respectively; their chemical compositions determined by inductively coupled plasma atomic emission spectroscopy (ICP-AES) are listed in Table S1. The Gd(2.5%)/LDHs displays series sharp (00*l*) reflections and the strong (003) reflection appears at 2θ 12.13°, indicating a typical CO_3^{2-}-LDHs phase with good crystallinity. As *x*% value rises from 5% to 20%, the (003) reflection of LDHs decreases obviously; new peaks in XRD assigned to $Gd(OH)_3$ are observed (Fig. S1a), and FT-IR spectra also show the absorption peak at 3616 cm^{-1} ascribed to $Gd(OH)_3$ (Fig. S1b) [37]. The increase of doped Gd^{3+} in Gd(*x*%)-LDH induces the increment of Zeta potential from +20.4 to +53.0 mV (Fig. S2 and Table S2). Taking into account the phase purity and crystallization, Gd(2.5%)-LDHs is chosen for the following study.

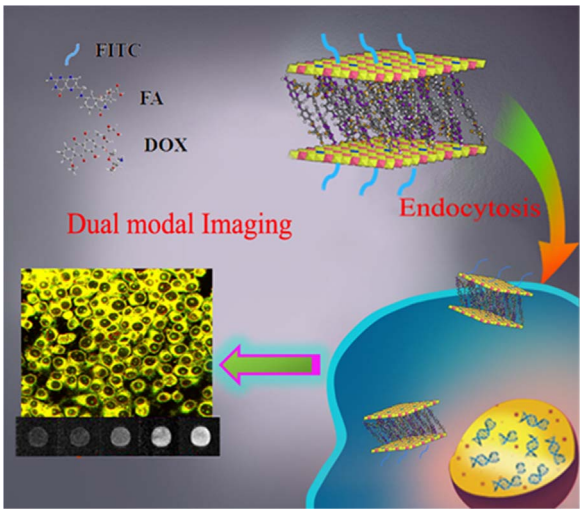

Scheme 1. Schematic illustration of FITC/FA-DOX/Gd-LDHs agent for dual-modal imaging and targeted chemotherapy.

We further optimized the loading amount of FITC, since its aggregation will result in fluorescence quenching and decrease the imaging ability. FITC is a derivative of fluorescein with an isothiocyanate group (–N=C=S), which takes the advantage of superior imaging performance without the deactivation of proteins compared with fluorescein. The FITC(*y*%)/Gd-LDHs samples are prepared and their fluorescence emission spectra are shown in Fig. S3c–e. The fluorescence intensity increases gradually from FITC(1%)/Gd-LDHs to FITC(5%)/Gd-LDHs, and then decreases from FITC(5%)/Gd-LDHs to FITC(25%)/Gd-LDHs owing to the aggregation of FITC. The sample of FITC(5%)/Gd-LDHs displays the maximum fluorescence intensity within the concentration range 15–400 μg/mL, and the fluorescence quantum yield of FITC(5%)/Gd-LDHs is 1.63 folds to protonated FITC and 31.1 folds to FITC at the concentration of 50 μg/mL (Fig. S3f). Therefore, FITC(5%)/Gd(2.5%)-LDHs is chosen as the optimum dual-modal imaging agent.

Monodispersed FITC/FA-DOX/Gd-LDH material was synthesized *via* SNAS method by incorporating DOX and FA into the Gd-LDH gallery. XRD pattern shows that the as-prepared FITC/Gd-LDH presents typical (00*l*) characteristic reflections with the (003) reflection at 2θ 10.18°, indicating FITC is mainly loaded on the surface rather than in the gallery (Fig. S4). After the co-incorporation of DOX and FA into the Gd-LDHs gallery, the (003) reflection of FITC/FA-DOX/Gd-LDH moves from 2θ 10.18° to 4.19° (Fig. 1a), with a corresponding basal spacing expansion from 0.86 nm to 2.21 nm, indicating FA and DOX are intercalated into the Gd-LDHs gallery. However, due to the high ratio of FA to LDHs (FA: LDHs=0.8), it is inevitable that part of FA is absorbed on the Gd-LDHs surface and results in the targeted drugs uptake. The incorporation of FITC, DOX and FA with the Gd-LDHs was studied by the FT-IR spectra (Fig. 1b). For the pristine Gd-LDHs, the band at 1375 cm^{-1} indicates a carbonate-type LDHs phase. As shown in Fig. 1b, the peak at 1606 cm^{-1} and 1401 cm^{-1} are attributed to the aromatic ring stretching of pteridine ring and *p*-amino benzoic acid of folic acid [26]. The vibrations at 1534 cm^{-1} and 1211 cm^{-1} are due to the C–O (phenolic) band and C–O–C band, respectively [38,39], demonstrating the presence of FITC. Moreover, the band at 1184 cm^{-1} corresponds to the $\delta(CH_3O–)$ stretching vibration of DOX [40]. The chemical composition of FITC/FA-DOX/Gd-LDHs is listed in Table S1. The energy dispersive spectrometer (EDS) (Fig. S5) proves the presence of Mg, Al, Gd, and S element, with a homogeneous dispersion confirmed by mapping image. SEM and HRTEM image (Fig. 1c and d) show hexagonal-like platelets with relatively uniform particle size. Dynamic light scattering (DLS) measurements give an average particle size of ~178 nm for FITC/FA-DOX/Gd-LDHs (Fig. S6f), which is suitable for permeability and retention (EPR) effect in the cell endocytosis [40,41]. As reference samples, Gd-LDHs and FITC/Gd-LDHs also illustrate uniform hexagonal platelets with particle size of ~98 nm and 107 nm, respectively (Fig. S6a–d).

The optical property of FITC/FA-DOX/Gd-LDHs was further investigated by the UV–vis absorption spectrometry (Fig. 2a). The pristine FITC shows a characteristic absorption peak at 490 nm, but its bandwidth broadens after incorporated with Gd-LDHs. After DOX is further intercalated into Gd-LDHs gallery, two typical peaks at 543 and 582 nm appear. For the FITC/FA-DOX/Gd-LDHs sample, an additional peak at 285 nm is observed compared with FITC/DOX/Gd-LDHs, originating from the absorption of FA. Fig. 2b displays the photoluminescence (PL) spectra of pristine FITC, FITC/Gd-LDHs, FITC/DOX/Gd-LDHs and FITC/FA-DOX/Gd-LDHs with the same DOX loading. Compared with pristine FITC in ethanol solution, a

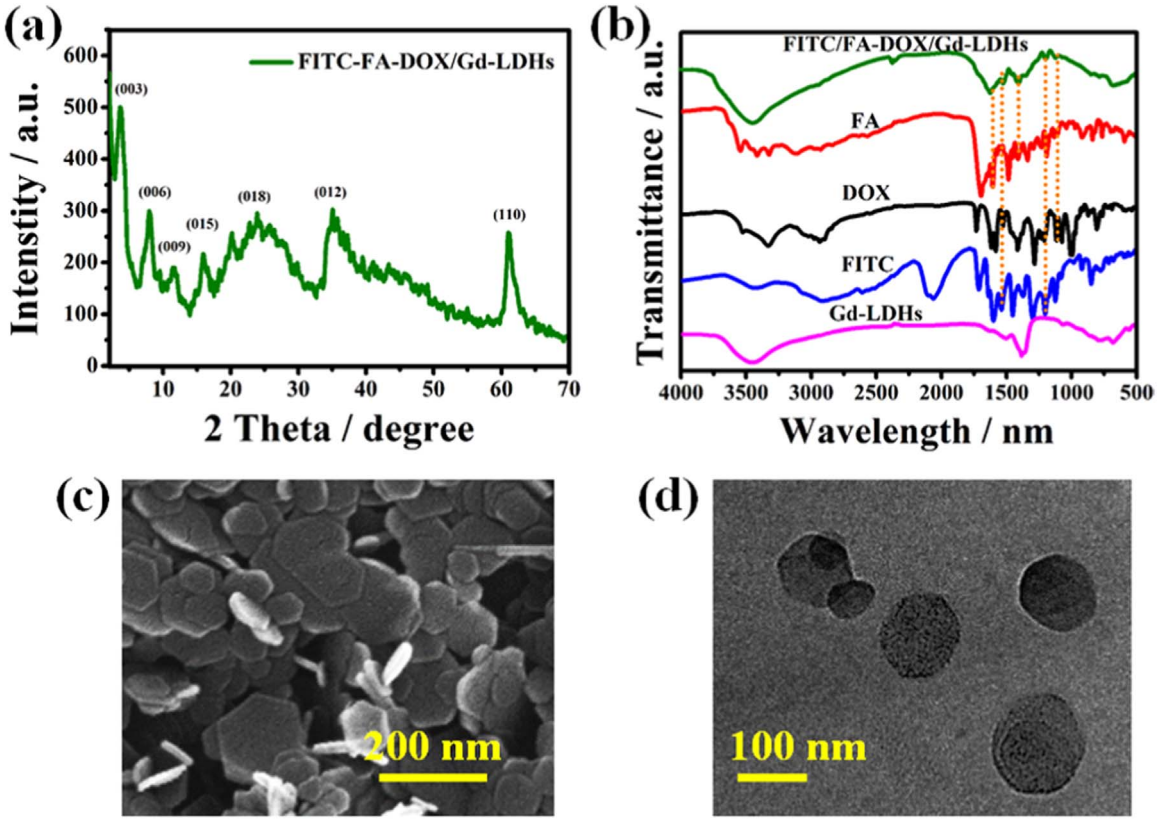

Fig. 1. (a) XRD pattern of FITC/FA-DOX/Gd-LDHs. (b) FTIR spectra of Gd-LDHs, FA, DOX, FITC and FITC/FA-DOX/Gd-LDHs, respectively. (c) SEM and (d) HRTEM image of FITC/FA-DOX/Gd-LDHs.

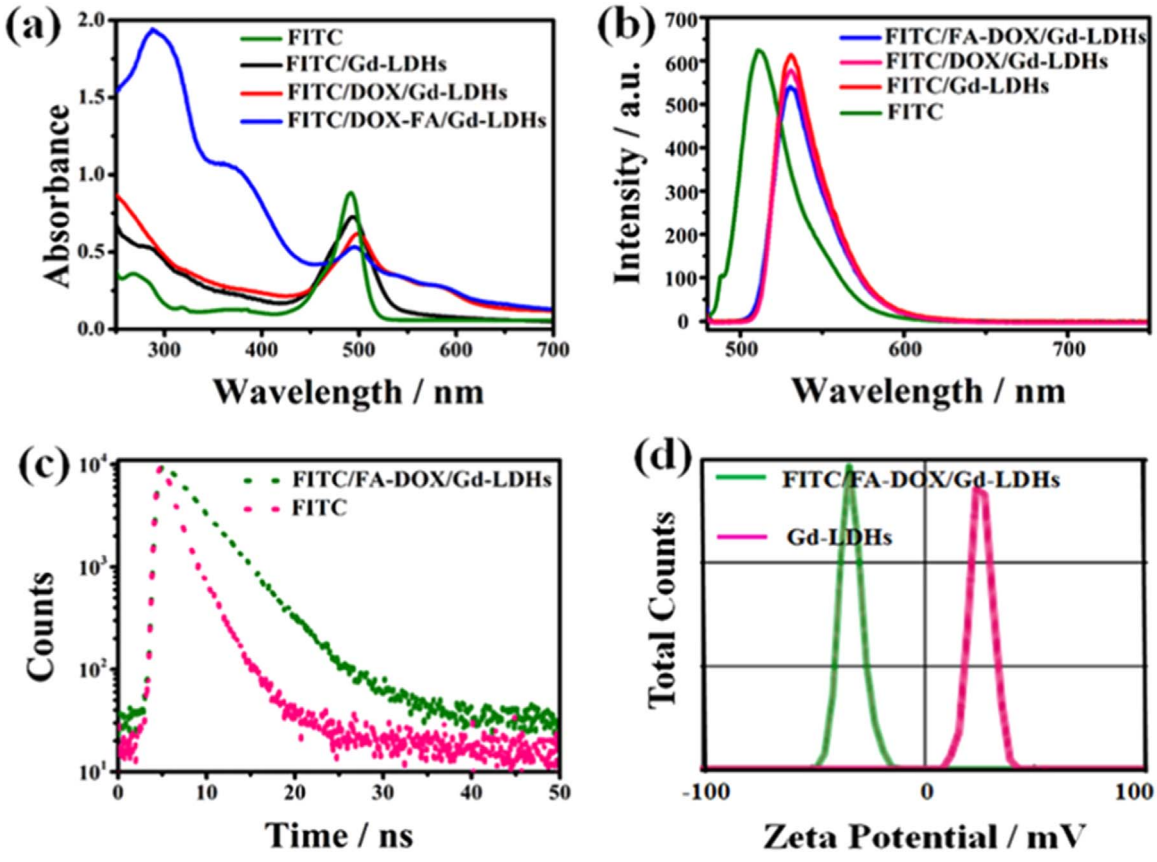

Fig. 2. (a) UV–vis and (b) Photoluminescence spectra of FITC ethanol solution, FITC/Gd-LDHs, FITC/DOX/Gd-LDHs and FITC/FA-DOX/Gd-LDHs, respectively. (c) Lifetime of FITC/FA-DOX/Gd-LDHs and pristine FITC. (d) Zeta potential of Gd-LDHs and FITC/FA-DOX/Gd-LDHs.

red-shift of 18 nm is observed for these three solid samples and the fluorescence lifetime of FITC/FA-DOX/Gd-LDHs (4.06 ns) increases markedly compared with that of pristine FITC (1.79 ns) (Fig. 2c, Table S3). This can be ascribed to the depressed mobility and internal conversion process of FITC due to the electrostatic and hydrogen-bonding interactions between FITC and the LDH host layer. It should be noted that the fluorescence intensity of FITC/DOX/Gd-LDHs and FITC/FA-DOX/Gd-LDHs decreases weakly relative to FITC/Gd-LDHs, indicating the intercalation of DOX and FA does not give a large influence on the fluorescence property. Moreover, the Gd-LDHs is positively-charged with a Zeta potential of +21.2 mV; while FITC/FA-DOX/Gd-LDHs is negatively-charged with −24.1 mV (Fig. 2d), indicating the incorporation of guest anions. The stability of FITC/FA-DOX/Gd-LDHs was tested by DLS over 9 days (Fig. S7), and the negligible variation in the particle size shows that it is desirable for long-time storage.

To further study the orientation and arrangement of the guests in the Gd-LDHs at atomic level, molecular dynamics (MD) simulations were performed on the sample of DOX(2%)-FA(80%)/Gd-LDHs. The structure model is constructed based on the results reported previously by our group [42]. The ratio Mg^{2+}/Al^{3+} is 2 and the unit cell parameters are $\alpha=\beta=90°$, $\gamma=120°$, $a=b=45$ Å, respectively. The molecular dynamics (MD) simulations were performed employing the force field of LDHFF3 in isothermal-isobaric (NPT) ensemble, with the temperature of 298 K and the pressure of 0.1 MPa. The structure model is composed of Mg (96), Al (43) and Gd (5) to keep the charge balance and Gd^{3+} is uniformly dispersed on the host layers (green color). Fig. 3 illustrates the probability distribution of the guests after the MD simulation: both the DOX and FA molecules are accommodated in the interlayer region in a slantwise state, with a slope angle (Fig. S8: the tail vector regarding to the host layer) of $\theta_1=70.40°$ and $\theta_2=45.92°$, respectively. The calculated d_{003} value is 20.6 Å, which is in approximately agreement with the XRD result (21.05 Å). Moreover, the distance between the carboxyl group in FA and the hydroxyl group in DOX is as short as ~2.0 Å, which is within the interaction range of hydrogen bonding.

2.2. Fluorescence imaging and MRI performance of FITC/FA-DOX/Gd-LDHs

Efficient internalization of cancer cells toward the layered material is of great importance for the cancer therapy, and the intake efficacy was firstly investigated through fluorescence imaging. KB cells were used to incubate with FITC/Gd-LDHs, FITC/DOX/Gd-LDHs and FITC/FA-DOX/Gd-LDHs respectively for 24 h, and their fluorescence images were recorded. The intrinsic fluorescence of FITC and DOX enables the independent imaging of KB cells. As shown in Fig. 4a–c, a strong green signal is observed when the cells are treated with FITC/Gd-LDHs, indicating its intake by the KB cells. For the FITC/DOX/Gd-LDHs, both the green signal of FITC and the red signal of DOX are detected in the KB cells (Fig. 4d–e). A yellow fluorescence signal (superimposition of green and red) is observed at cell cytoplasm (Fig. 4f), manifesting that the FITC/DOX/Gd-LDHs is located in the cell cytoplasm. In the case of FITC/FA-DOX/Gd-LDHs, the fluorescence signal can also be detected in the cell cytoplasm, and its intensity

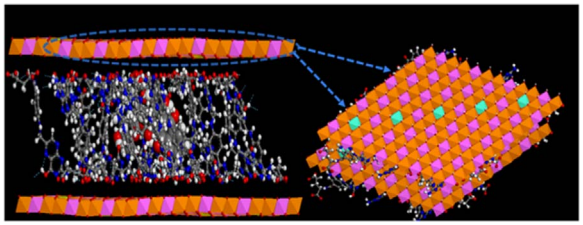

Fig. 3. The model geometry of FA-DOX/Gd-LDHs by MD simulation.

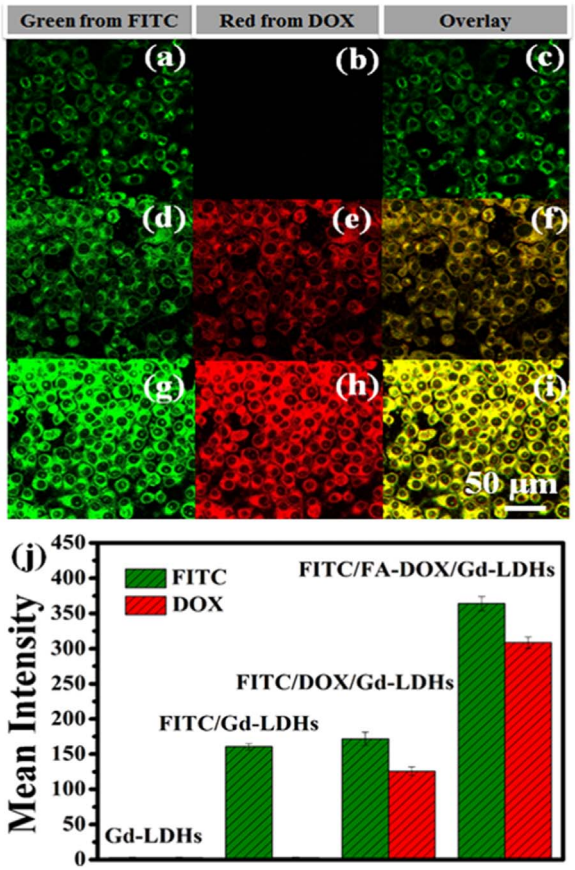

Fig. 4. *In vitro* confocal analysis images of KB cell incubated with (a–c) FITC/Gd-LDHs, (d–f) FITC/DOX/Gd-LDHs and (g–i) FITC/FA-DOX/Gd-LDHs for 24 h. (j) Fluorescence intensity of Gd-LDHs, FITC/Gd-LDHs, FITC/DOX/Gd-LDH and FITC/FA-DOX/Gd-LDHs, respectively.

is significantly heightened relative to FITC/Gd-LDHs and FITC/DOX/Gd-LDHs (Fig. 4g–i). Moreover, the average pixels of imaging zones can be calculated, and the fluorescence intensity of FITC/FA-DOX/Gd-LDHs in the cytoplasm is 2.11-folds stronger than that of FITC/DOX/Gd-LDHs (364 *vs* 172) with the concentration of 10 μg/mL (Fig. 4j), indicating the best intake performance as a result of the targeting ability of FA toward KB cells. Furthermore, we further studied the uptake time of KB cells toward FITC/FA-DOX/Gd-LDHs. An incubation time of 24 h allows strong green and red fluorescence signals, which is necessary for fluorescence imaging (Fig. S9). In addition, a similar result can also be found in HepG-2 cancer cells (Fig. S10), revealing the targeting uptake ability of FITC/FA-DOX/Gd-LDHs sample.

The dual-modal imaging based on combination of MRI and fluorescence has made great contribution to the enhancement of sensitivity and accuracy. Due to the high-spin Gd^{3+} with seven unpaired electrons on the host layers of FITC/FA-DOX/Gd-LDHs, straight water coordination with Gd^{3+} is conducive to trigger the longitudinal relaxivity [34,46]. To examine the MRI properties of FITC/FA-DOX/Gd-LDHs, a T_1-weighted MR imaging was performed on a 3.0 T Siemens Magnetom Trio system with a 0.5 T magnetic field. Tubes containing the FITC/FA-DOX/Gd-LDHs colloid were arrayed in an order of increased Gd^{3+} concentration, and water was used as a control sample. As shown in Fig. 5 inset, a positive enhancement of MRI signal is observed for these samples, and T_1-weighted MR images brighten increasingly with the increment of Gd^{3+} concentration. Fig. 5 displays a linear correlation between the longitudinal relaxation rate ($1/T_1$) and Gd^{3+} concentration, and the r_1 value of the FITC/FA-DOX/Gd-LDHs is measured to be 6.22 mM^{-1} s^{-1}. This indicates the potential

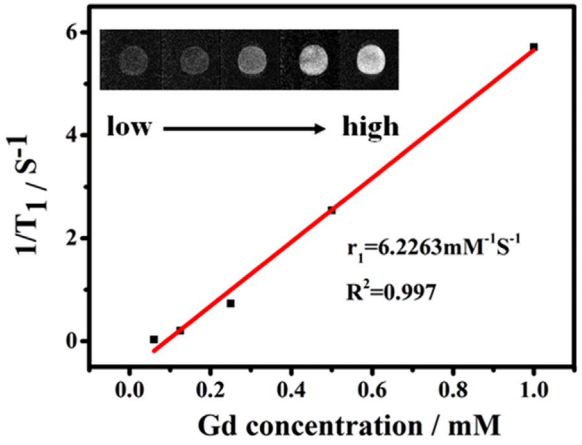

Fig. 5. Magnetic resonance imaging (MRI) of FITC/FA-DOX/Gd-LDHs.

application of FITC/FA-DOX/Gd-LDHs as an MRI contrast agent. Nevertheless, it is very regretful that the MRI imaging *in vitro* can't be performed due to the limit of instrument and further study is in progress. Although the r_1 value of FITC/FA-DOX/Gd-LDHs (6.22 mM^{-1} s^{-1}) is lower than that of Gd chelates (9.90–36.0 mM^{-1} s^{-1}) [43–46], it is larger than that of doped Gd nanoparticles (1.40–6.18 mM^{-1} s^{-1}) [47,48] and clinical MRI agent (4.10 mM^{-1} s^{-1}). Moreover, the FITC/FA-DOX/Gd-LDHs sample shows the advantages of targeted uptake and EPR retention, which can serve as a prospective MRI contrast agent.

2.3. In vitro *anticancer activity*

The anticancer activity of FITC/FA-DOX/Gd-LDHs was further studied by *in vitro* tests performed with KB cells. The cytotoxicity of Gd-LDHs and FITC/Gd-LDHs was firstly studied (Fig. S11), and cell viability maintained 100% and 98.2% in the presence of Gd-LDHs and FITC/Gd-LDHs (concentration as high as 100 μg/mL), respectively, indicating a good biocompatibility of the drug carrier. Subsequently, the KB cells were incubated with FITC/DOX/Gd-LDHs, FITC/FA-DOX/Gd-LDHs and pristine DOX with equivalent DOX concentration ranging from 0.3 to 20 μg/mL for 24 h, washed thoroughly with PBS, and then determined by the CCK-8 assay. As shown in Fig. 6a, a significant anticancer effect occurs and enhances gradually along with the increase of dosage from 0.3 to 20 μg/mL. The FITC/DOX/Gd-LDHs and FITC/FA-DOX/Gd-LDHs show a half-maximal inhibitory concentration (IC_{50}) of 28.73 μg/mL and 9.53 μg/mL, respectively, which is larger than that of pristine DOX (6.36 μg/mL). This is due to the rapid uptake of DOX while both the other two LDHs samples undergo an uptake-delivery-release procedure [49]. In comparison with FITC/DOX/Gd-LDHs, the anticancer efficacy of FITC/FA-DOX/Gd-LDHs is remarkably enhanced *via* conjugation with FA, demonstrating the effectiveness of FA toward specifically targeting KB cells. Furthermore, we investigated the anticancer activity of these three samples with various drug concentrations at 48 h (Fig. 6b). Based on the CCK-8 assay, the IC_{50} of DOX, FITC/DOX/Gd- LDHs and FITC/FA-DOX/Gd-LDHs is 3.23, 12.01 and 5.00 μg/mL, respectively, confirming an enhanced anticancer performance with prolonged incubation time. Moreover, the cytotoxicity of the Gd-LDH, FITC/DOX/Gd-LDHs, FITC/FA-DOX/Gd-LDHs, and pristine DOX toward L02 (normal liver cells) cells were also investigated. According to the CCK-8 results (Fig. S12), the viability reveals that L02 cells show a strong tolerance to FITC/FA-DOX/Gd-LDHs with the viability of 58.21% (DOX=10 μg/mL), while pristine DOX displays a much stronger cytotoxicity (viability=9.00%) at the equivalent concentration. Therefore, although FITC/FA-DOX/Gd-LDHs and DOX exhibit close anticancer effectiveness, the former shows a weak cytotoxicity and largely enhanced biocompatibility, as a result of the incorporation of LDHs nanovehicle.

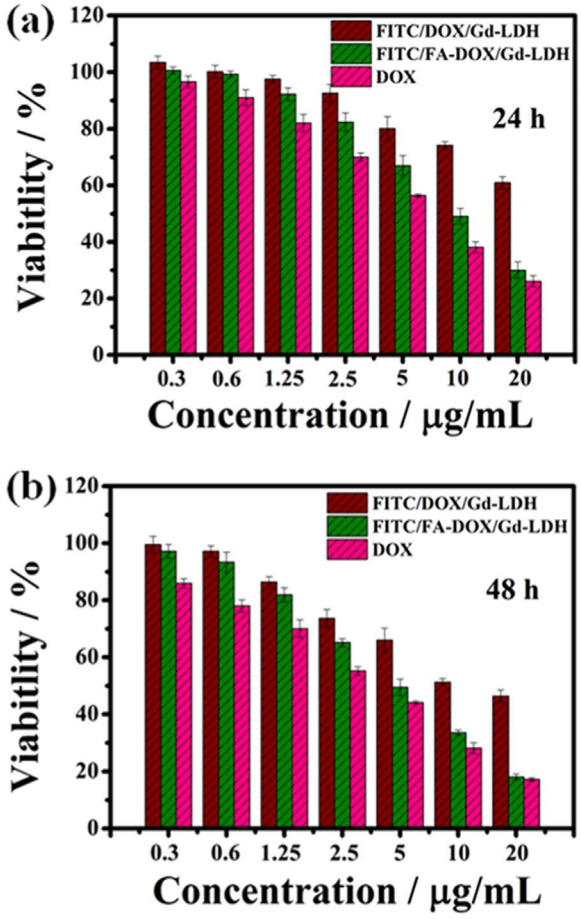

Fig. 6. Cell viability of KB cells incubated with FITC/DOX/Gd-LDHs, FITC/FA-DOX/Gd-LDHs, and pristine DOX after (a) 24 h and (b) 48 h, respectively.

3. Conclusions

In summary, a novel supramolecular nanovehicle was fabricated by the co-intercalation of FA and DOX into Gd^{3+}- doped LDH, followed by the adsorption of FITC. The FITC/FA-DOX/Gd-LDHs presents uniform morphology with particle size of ~178 nm and superior stability. Moreover, this material demonstrates dual-modal imaging based on fluorescence signal from FITC and MRI from Gd^{3+} in LDHs host layers. *In vitro* experiments show that the FITC/FA-DOX/Gd-LDHs exhibits an obviously increased targeting uptake and anticancer activity toward KB cells. Therefore, this work demonstrates a drug formulation paradigm by combination of fluorescence imaging and MRI agent, chemotherapeutic drug into LDHs nanovehicle, which would serve as a promising candidate in dual-modal imaging and targeted chemotherapy.

4. Experimental

4.1. Reagents and materials

Chemicals including $Gd(NO_3)_3{\cdot}6H_2O$, $Mg(NO_3)_2{\cdot}6H_2O$, $Al(NO_3)_3{\cdot}9H_2O$, DOX, FITC and FA, were purchased from Aladdin company. NaOH, acetone, ethanol were obtained from the Beijng Chemical Co., Ltd. Corporation. All the chemicals were analytical grade and used without further purification. DMEM (Dulbecco's modified eagle medium), FBS (fetal bovin serum), PBS (Phosphate buffer solution) were

purchased from Beijing Solarbio Science and Technology Company. A Cell Counting Kit-8 (CCK-8) was purchased from Doindo Laboratories (Japan). KB cells were obtained from the Institute of Basic Medical Sciences Chinese Academy of Medical Sciences. Deionized water was used throughout the experimental processes.

4.2. Synthesis of FITC/FA-DOX/Gd-LDHs

FITC/FA-DOX/Gd-LDHs was prepared based on the SNAS method reported by our group. Typically, 40 ml of solution A ($Mg(NO_3)_2{\cdot}6H_2O$: 0.003 mol; $Al(NO_3)_3{\cdot}9H_2O$: 0.0015 mol and $Gd(NO_3)_3{\cdot}9H_2O$: 3.75×10^{-5} mol; DOX: 3×10^{-5} mol) and 40 ml of solution B (NaOH: 0.01 mol and FA: 0.0012 mol) were simultaneously added to a colloid mill with rotor speed of 3500 rpm and mixed for 1 min. The aqueous suspension was transferred into a three-neck bottle with the N_2 protection. During this period, the FITC solution was added to the aqueous suspension of FA-DOX/Gd-LDHs. After hydrothermal treatment at 60 °C for 24 h, the obtained slurry was centrifuged three times with water and ethanol, respectively, follow by dried in the 60 °C oven overnight.

4.3. In vitro cell assay

To study the integrated performance of DOX, FITC/DOX/Gd-LDHs, and FITC/FA-DOX/Gd-LDHs, KB cells were used to evaluate their anticancer activity. Specifically, KB cells were cultured and expanded in 25 cm^2 cell-culture flask. After reaching 80–90% confluence, the KB cells were washed with PBS, afterwards detached from the flask by addition of 1.0 mL of 0.25% trypsin for 1–3 min at 37 °C. KB cells (1×10^4 cells/well) were seeded into two 96-well plates, respectively. After further incubation of 24 h, pristine DOX, FITC/DOX/Gd-LDHs and FITC/FA-DOX/Gd-LDHs with concentration ranging from 0.3–20 μg/mL were added into the wells and incubated for 24 h, respectively. After washing three times with PBS, the mixture of CCK-8 and DMEM (1:10) was added to 96-well plates for the determination of cell viability.

4.4. Sample characterization

X-ray diffraction (XRD) patterns were recorded by a Rigaku XRD-6000 diffractometer, using Cu Kα radiation (λ=0.15418 nm) at 40 kV, 30 mA. The photoluminescence spectra were tested on a RF-5301PC fluorospectrophotometer with the 490 nm excitation wavelength. UV–vis absorption spectra were collected in the range 200–700 nm on a Shimadzu U-3000 spectrophotometer, with the slit width of 1.0 nm. The multiple-exponentially fitting using Edinburgh F980 instrument software calculated the fluorescence decays were obtained on Edinburgh Instruments FLS980 fluorimeter and the average fluorescence lifetime. The morphology of composites was investigated by SEM (Zeiss SUPRA 55) with the accelerating voltage of 20 kV. Transmission electron microscopy (TEM) images were recorded with JEOL JEM-2010 high resolution transmission electron microscopes and the accelerating voltage was 200 kV. The Fourier Transform Infrared spectra (FT-IR) were obtained using a Vector 22 (Bruker) spectrophotometer in the range 4000–400 cm^{-1} with 2 cm^{-1} resolution. The chemical compositions of the composites were determined by inductively coupled plasma atomic emission spectrometry (ICP-AES). Biotek synergy H_1 was applied to investigate the cell viability. Fluorescence images were obtained using a confocal microscope (Leica TCS-SP5) with the 60×oil-immersion objective. The longitudinal relaxation time (T_1) of FITC/FA-DOX/Gd-LDHs solution was measured by a Magritek NMR Analyzer at room temperature with varied Gd^{3+} concentration and the MRI was performed on the Terranova-MRI.

Supporting information

XRD patterns and FTIR spectra of Gd(x%)-LDHs (x ranges from 2.5% to 20%) are shown in Fig. S1. Zeta potential of Gd(x%)-LDHs (x ranges from 2.5% to 20%) is displayed in Fig. S2. Photoluminescence spectra of FITC(y%)/Gd-LDHs (y ranges from 1% to 25%) are shown in Fig. S3. XRD patterns of FITC(y%)/Gd-LDHs are displayed in Fig. S4. EDS mapping of the FITC/FA-DOX/Gd-LDHs is illustrated in Fig. S5. SEM images and Dynamic lighting scatting (DLS) results of Gd-LDHs, FITC/Gd-LDHs and FITC/FA-DOX/Gd-LDH are recorded in Fig. S6. DLS results of FITC/FA-DOX/Gd-LDHs are shown in Fig. S7. Distribution of tilt angle θ_1 of FA and θ_2 of DOX regarding to hydroxide sheets in the MD simulation models is shown in Fig. S8. *In vitro* confocal analysis images of KB cell incubated with FITC/FA-DOX/Gd-LDHs for 3 h and 24 h are displayed in Fig. S9. The fluorescence images of HepG-2 cell incubated with FITC/DOX/Gd-LDHs and FITC/FA-DOX/Gd-LDHs were revealed in Fig. S10. Cell viability of Gd-LDHs and FITC/Gd-LDHs incubated with KB for 24 h is shown in Fig. S11. Cell viability of L02 cells incubated with Gd-LDH, FITC/DOX/Gd-LDHs, FITC/FA-DOX/Gd-LDHs, and pristine DOX for 24 h is shown in Fig. S12.

Acknowledgements

This work was supported by the 973 Program (Grant No. 2014CB932103), the National Natural Science Foundation of China (NSFC, 21601010), the Innovation and Promotion Project of Beijing University of Chemical Technology (buctrc201611) and the Fundamental Research Funds for the Central Universities (YS 1406).

Appendix A. Supporting information

Supplementary data associated with this article can be found in the online version at doi:10.1016/j.talanta.2016.12.068.

References

[1] Y. Wang, S. Song, J. Liu, D. Liu, H. Zhang, Angew. Chem. Int. Ed. 54 (2015) 536–540.
[2] Y. Li, T.Y. Lin, Y. Luo, Q. Liu, W. Xiao, W. Guo, D. Lac, H. Zhang, C. Feng, S.W. Hogiu, J.H. Walton, S.R. Cherry, D.J. Rowland, D. Kukis, C. Pan, K.S. Lam, Nat. Commun. 5 (2014) 4712–4716.
[3] H. Zhang, H. Wu, J. Wang, Y. Yang, D. Wu, Y. Zhang, Y. Zhang, Z. Zhou, S. Yang, Biomaterials 42 (2015) 66–77.
[4] L. Wang, X. Zhu, X. Tang, C. Wu, Z. Zhou, C. Sun, S.L. Deng, H. Ai, J. Gao, Chem. Commun. 51 (2015) 4390–4393.
[5] L. Li, L. Zhang, T. Wang, X. Wu, H. Ren, C. Wang, Z. Su, Small 11 (2015) 3162–3173.
[6] G. Tian, X. Zheng, X. Zhang, W. Yin, J. Yu, D. Wang, Z. Zhang, X. Yang, Z. Gu, Y. Zhao, Biomaterials 40 (2015) 107–116.
[7] M. Zhou, J. Li, S. Liang, A.K. Sood, D. Liang, C. Li, ACS Nano 9 (2015) 7085–7096.
[8] X. Cao, F. Cao, L. Xiong, Y. Yang, T. Cao, X. Cai, W. Hai, B. Li, Y. Guo, Y. Zhang, F. Li, Nanoscale 7 (2015) 13404–13409.
[9] J. Mou, P. Li, C. Liu, H. Xu, L. Song, J. Wang, K. Zhang, Y. Chen, J. Shi, H. Chen, Small 11 (2015) 2275–2283.
[10] M. Sun, L. Xu, W. Ma, X. Wu, H. Kuang, L. Wang, C. Xu, Adv. Mater. 28 (2016) 898–904.
[11] X. Bai, S. Xu, J. Liu, L. Wang, Talanta 150 (2016) 118–124.
[12] X. Zhu, J. Zhou, M. Chen, M. Shi, W. Feng, F. Li, Biomaterials 33 (2012) 4618–4627.
[13] N. Lee, H.R. Cho, M.H. Oh, S.H. Lee, K. Kim, B.H. Kim, K. Shin, T.Y. Ahn, J.W. Choi, Y.W. Kim, S.H. Choi, T. Hyeon, J. Am. Chem. Soc. 134 (2012) 10309–10312.
[14] H.J. Cho, H.Y. Yoon, H. Koo, S.H. Ko, J.S. Shim, J.H. Cho, J.H. Park, K. Kim, I.C. Kwon, D.D. Kim, J. Control. Release 162 (2012) 111–118.
[15] K. Deng, Z. Hou, X. Li, C. Li, Y. Zhang, X. Deng, Z. Cheng, J. Lin, Sci. Rep. 5 (2015) 7851–7858.
[16] F. Peng, Y. Su, X. Wei, Y. Lu, Y. Zhou, Y. Zhong, S.T. Lee, Y. He, Angew. Chem. Int. Ed. 52 (2013) 1457–1461.
[17] Y. Wang, K. Wang, J. Zhao, X. Liu, J. Bu, X. Yan, R. Huang, J. Am. Chem. Soc. 135 (2013) 4799–4804.
[18] P. Zhang, J. Kong, Talanta 134 (2015) 501–507.
[19] Z. Zhang, J. Wang, X. Nie, T. Wen, Y. Ji, X. Wu, Y. Zhao, C. Chen, J. Am. Chem. Soc. 136 (2014) 7317–7326.

[20] Q. Chen, C. Liang, X. Wang, J. He, Y. Li, Z. Liu, Biomaterials 35 (2014) 9355–9362.
[21] X. Cui, S. Belo, D. Krüger, Y. Yan, R.T.M. Rosales, M.J. Osoro, H. Ye, S. Su, D. Mathe, N. Kovács, I. Horváth, M. Semjeni, K. Sunassee, K. Szigeti, M.A. Green, P.J. Blower, Biomaterials 35 (2014) 5840–5846.
[22] L. Chen, L. Li, L. Zhang, S. Xing, T. Wang, Y.A. Wang, C. Wang, Z. Su, A.C.S. Appl, Mater. Interfaces 5 (2013) 7282–7290.
[23] J. Li, Y. Hu, J. Yang, P. Wei, W. Sun, M. Shen, G. Zhang, X. Shi, Biomaterials 38 (2015) 10–21.
[24] J. Croissant, M. Maynadier, O. Mongin, V. Hugues, M.B. Desce, A. Chaix, X. Cattoën, M.W. Man, A. Gallud, M.G. Bobo, Small 11 (2015) 295–299.
[25] Z. Zhang, P. Zhang, K. Guo, G. Liang, H. Chen, B. Liu, J. Kong, Talanta 85 (2011) 2695–2699.
[26] D. Yin, S. Cui, Y. Chen, Y. Di, H. Chen, Y. Ma, S. Achilefu, Y. Gu, ACS Nano 7 (2013) 676–688.
[27] X. Zhu, W. Feng, J. Chang, Y.W. Tan, J. Li, M. Chen, Y. Sun, F. Li, Nat. Commun. 7 (2016) 1–10.
[28] Q. Han, Z. Wang, J. Xia, S. Chen, X. Zhang, M. Ding, Talanta 101 (2012) 388–395.
[29] W. Chen, B. Zhang, T. Mahony, W. Gu, B. Rolfe, Z.P. Xu, Small 12 (2016) 1627–1639.
[30] F.Y. Southworth, C. Wilson, S.J. Coles, A.M. Fogg, Dalton Trans. 43 (2014) 10451–10455.
[31] Q. Wang, D. O'Hare, Chem. Rev. 112 (2012) 4124–4155.
[32] W. Shi, X. Ji, S. Zhang, M. Wei, D.G. Evans, X. Duan, J. Phys. Chem. C 115 (2011) 20433–20441.
[33] S.J. Choi, G.E. Choi, J.M. Oh, Y.J. Oh, M.C. Park, J.H. Choy, J. Mater. Chem. 20 (2010) 9463–9465.
[34] L. Wang, H. Xing, S. Zhang, Q. Ren, L. Pan, K. Zhang, W. Bu, X. Zheng, L. Zhou, W. Peng, Y. Hua, J. Shi, Biomaterials 34 (2013) 3390–3401.
[35] W.M. Kriven, S.Y. Kwak, M.A. Wallig, J.H. Choy, MRS Bull. 29 (2004) 33–37.
[36] Y. Zhao, F. Li, R. Zhang, D.G. Evans, X. Duan, Chem. Mater. 14 (2002) 4286–4291.
[37] Y. Yang, Y. Sun, Y. Liu, J. Peng, Y. Wu, Y. Zhang, W. Feng, F. Li, Biomaterials 34 (2013) 508–515.
[38] R. Khandelia, A. Jaiswal, S.S. Ghosh, A. Chattopadhyay, Small 9 (2013) 3494–3505.
[39] S. Li, J. Li, C.J. Wang, Q. Wang, M.Z. Cader, J. Lu, D.G. Evans, X. Duan, D. O'Hare, J. Mater. Chem. B 1 (2013) 61–68.
[40] S. Guan, R. Liang, C. Li, D. Yan, M. Wei, D.G. Evans, X. Duan, J. Mater. Chem. B 4 (2016) 1331–1336.
[41] A.B. Attia, P. Oh, C. Yang, J.P. Tan, N. Rao, J.L. Hedrick, Y.Y. Yang, R. Ge, Small 10 (2014) 4281–4286.
[42] D. Yan, J. Lu, J. Ma, S. Qin, M. Wei, D.G. Evans, X. Duan, Angew. Chem. Int. Ed. 50 (2011) 7037–7040.
[43] K.W. Hu, K.C. Hsu, C.S. Yeh, Biomaterials 31 (2010) 6843–6848.
[44] X. Hu, G. Liu, Y. Li, X. Wang, S. Liu, J. Am. Chem. Soc. 137 (2015) 362–368.
[45] J.Y. Park, M.J. Baek, E.S. Choi, S. Woo, J.H. Kim, T.J. Kim, J.C. Jung, K.S. Chae, Y. Chang, G.H. Lee, ACS Nano 3 (2009) 3663–3669.
[46] L.M. Manus, R.C. Strauch, A.H. Hung, A.L. Eckermann, T.J. Meade, Anal. Chem. 84 (2012) 6278–6287.
[47] Y.I. Park, J.H. Kim, K.T. Lee, K.S. Jeon, H.B. Na, J.H. Yu, H.M. Kim, N. Lee, S.H. Choi, S.I. Baik, Adv. Mater. 21 (2009) 4467–4471.
[48] F. Chen, W. Bu, S. Zhang, X. Liu, J. Liu, H. Xing, Q. Xiao, L. Zhou, W. Peng, L. Wang, J. Shi, Adv. Funct. Mater. 21 (2011) 4285–4294.
[49] J.M. Oh, S.J. Choi, S.T. Kim, J.H. Choy, Bioconjugate Chem. 17 (2006) 1411–1417.